Correspondence to:

M. Lindberg,
mli6@kth.se

Fermi Acceleration of Electrons at Earth's Bow Shock Due To Current Sheet Interaction

M. Lindberg[1] , X. Shi[2] , H. Hietala[1] , L. Vuorinen[1] , S. Raptis[3] , F. Koller[1] , and A. Lalti[4]

[1]Department of Physics and Astronomy, Queen Mary University of London, London, UK, [2]Department of Earth, Planetary, and Space Sciences and Institute of Geophysics and Planetary Physics, University of California, Los Angeles, CA, USA, [3]The Johns Hopkins University Applied Physics Laboratory, Laurel, MD, USA, [4]Northumbria University, Newcastle upon Tyne, UK

Abstract We use the Magnetospheric Multiscale (MMS) mission to present a case study of electron acceleration at Earth's bow shock due to an interaction with a solar wind magnetic depression. The magnetic depression is identified as a reconnecting current sheet and is observed both at the bow shock, using MMS, and upstream of the shock at the Lagrange point 1 using the ACE, WIND, and DSCOVR spacecraft. The interaction with the current sheet and drop in magnetic field magnitude enables electrons to be accelerated from thermal energies (10–20 eV) up to suprathermal energies (1–5 keV) in a process producing a power-law with a spectral index $p = -2.3$ close to that predicted by first order Fermi acceleration ($p = -2$). The observations are compared to a numerical model of Fermi acceleration considering two approaching magnetic mirrors and pitch angle scattering by whistler waves, and good agreement is shown. Thus, we add another piece to resolving the long-standing electron injection problem.

1. Introduction

Collisionless shock waves are ubiquitous throughout our universe (Bykov & Treumann, 2011) and constitute important sources of plasma heating and particle acceleration (Giacalone, 2005; Goodrich & Scudder, 1984; Johlander et al., 2021; Perri et al., 2022). It has been shown that cosmic rays, one of the most energetic particles in the universe, are accelerated to ultra-relativistic energies at astrophysical shocks found at supernova remnants (Bamba et al., 2005; Koyama et al., 1995). They are believed to be accelerated through Diffusive Shock Acceleration (DSA), also called first-order Fermi-acceleration (Blandford & Eichler, 1987; Drury, 1983; Longair, 1981). However, the DSA theory requires particles to be pre-accelerated up to a certain injection threshold energy before they can be injected into the DSA process and gain immense energy.

While ion injection into DSA is sufficiently well understood, electron injection remains, to a greater extent, an open question (Amano & Hoshino, 2022; Levinson, 1992). The much smaller mass of the electrons (compared to ions) inherently gives rise to a much higher electron injection threshold, requiring electrons to reach at least mildly relativistic energies (10–100 keV) before being injected. Therefore, the lack of a process capable of consistently accelerating electrons from thermal energies (10–20 eV) up to relativistic energies is called the electron injection problem and much effort has been made to find a solution over the past decades.

Shock Drift Acceleration (SDA) is a common acceleration mechanism at collisionless shocks (Ball & Melrose, 2001; Wu, 1984). However, it is not efficient to generate the observed fluxes of mildly relativistic electrons typically measured at shocks (Vandas, 2001; Webb et al., 1983). The Stochastic Shock Drift Acceleration (SSDA) is currently the most promising candidate for resolving the electron injection problem (Amano & Hoshino, 2022). It adds a stochastic component to the SDA mechanism through pitch angle scattering by plasma waves in the shock transition. The wave scattering enables electrons to undergo the SDA process longer and reach higher energies. Theoretical work (Katou & Amano, 2019), supported by observational evidence (Amano et al., 2020; Lindberg et al., 2024), suggests that the maximum energy obtainable via the SSDA mechanism depends on the pitch angle scattering (diffusion) rate of the electrons and therefore underlines the importance of the presence of suitable wave modes able to scatter electrons within the shock acceleration region. However, there is no single wave mode capable of pitch angle scattering electrons from thermal energies up to relativistic energies (Amano & Hoshino, 2022; Shi et al., 2025). Previous studies show that cyclotron resonance with whistler waves in the shock transition can provide sufficient scattering but typically only for suprathermal electrons (> 1 keV) (Amano

et al., 2020). For SSDA to successfully explain thermal electron acceleration, the theory needs to provide a mechanism for pitch angle scattering at thermal electron energies. This is still an open question, but electrostatic wave interactions have recently been shown to be a promising candidate (Kamaletdinov et al., 2022; Shi et al., 2025; Vasko et al., 2018).

Recent studies extend the electron acceleration region (EAR) away from the shock transition region by considering an interplay between the shock itself and upstream foreshock transients (Raptis, Lalti, et al., 2025; Shi et al., 2025). While SDA and SSDA are typically only efficient at quasi-perpendicular shocks, recent observations show instances of energetic electrons reaching 100–500 keV in the foreshock of Earth's quasi-parallel bow shock (Liu et al., 2019; Raptis, Lalti, et al., 2025; Raptis, Lindberg, et al., 2025; D. Turner et al., 2018; Wilson et al., 2016). Liu et al. (2017) and Shi et al. (2025) suggest that upstream foreshock transients, as they are convecting toward the shock, can act like magnetic mirrors and reflect (trap) electrons in a Fermi acceleration process between the upstream transients and the shock.

In this study, we directly observe the interaction between an upstream solar wind magnetic depression and Earth's bow shock, leading to electron acceleration from thermal energies (10–20 eV) up to suprathermal energies (1–5 keV). Using multi-spacecraft observations, the magnetic depression is identified as a reconnecting current sheet (RCS) impinging on the shock. We show that the RCS geometry and the steep drop in magnetic field create an ideal set of conditions for the thermal electrons to be energized via a transient Fermi mechanism. Moreover, the observations are compared to a Fermi-acceleration numerical model, described in Shi et al. (2025), considering two approaching magnetic mirrors and pitch angle scattering by whistler waves.

2. Observations

2.1. Magnetospheric Multiscale (MMS) Observations

Figure 1 shows an overview of two shock crossings observed by the Magnetospheric Multiscale (MMS) mission (Burch et al., 2016) on the 20th of November 2018. The first crossing is observed at around 09:26:00 UT, crossing the shock from downstream to upstream. As MMS exits the downstream magnetosheath into the shock ramp and eventually foot region (09:25:50–09:26:30 UT), MMS1 measures an unusually low magnetic field magnitude (see Figure 1a) of just above 1 nT. At the same time, a large increase in the electron differential energy flux is observed for energies between 100 eV and 1 keV (Figure 1c). After the magnetic field strength reaches its lowest value, near the start of the shock foot (blue marked region in Figures 1 and 2), MMS1 encounters a steep rise in the magnetic field (a magnetic wall) around 09:26:25 UT. MMS1 then briefly entered the solar wind around 09:26:30 UT before returning to an extended foot region of Earth's bow shock comprised of magnetic fluctuations observed between 09:26:35 and 09:28:30 UT before eventually crossing Earth's bow shock again at roughly 09:28:35 UT into the downstream magnetosheath. Figure 1g shows the MMS location in the near-Earth environment in the Geocentric Solar Ecliptic XY-plane and upstream magnetic field direction obtained from the OMNI database (King & Papitashvili, 2005).

In Figure 2 we present a zoomed-in view of the shock crossing of interest in this study (blue; the left shock depicted in Figure 1), henceforth referred to as the shock of interest. The right shock crossing in Figure 1 will be used mainly for comparison purposes and will therefore be referred to as the comparison shock crossing (red).

As mentioned above, the region between the shock and the upstream magnetic wall (09:25:55–09:26:25 UT) shows enhanced electron flux up to 1–5 keV accompanied by a large increase in mid to high frequency (0.02–0.2 of the electron cyclotron frequency f_{ce}) whistler wave activity (see Figures 1b, 1c, 2b, and 2c) throughout the whole region which we will refer to as the EAR. The prominent red band present around 20 Hz in Figures 1b and 2b is an instrumental artifact, and data from this frequency channel has been omitted in our analysis. In Figure 2d, we show the wave normal angle θ_{Bk} spectrum obtained using singular value decomposition (Santolík et al., 2003). We see that the whistler waves inside the EAR are obliquely propagating with an average around 47° and a standard deviation of 22° for the blue shaded interval.

In Figure 2g, we show the phase-space density (distribution function) of electrons, averaged over solid angle, for three time stamps within the EAR (black, brown, and mustard yellow) and one time stamp in the solar wind (gray) for reference. The electron phase space density profiles within the EAR are observed to form distinct power-laws at the suprathermal energies between 200 eV up to 1 keV before starting to fall off in a cut-off and eventually hitting the noise floor (faded data points and dotted lines in Figure 2g). The suprathermal power-laws show an
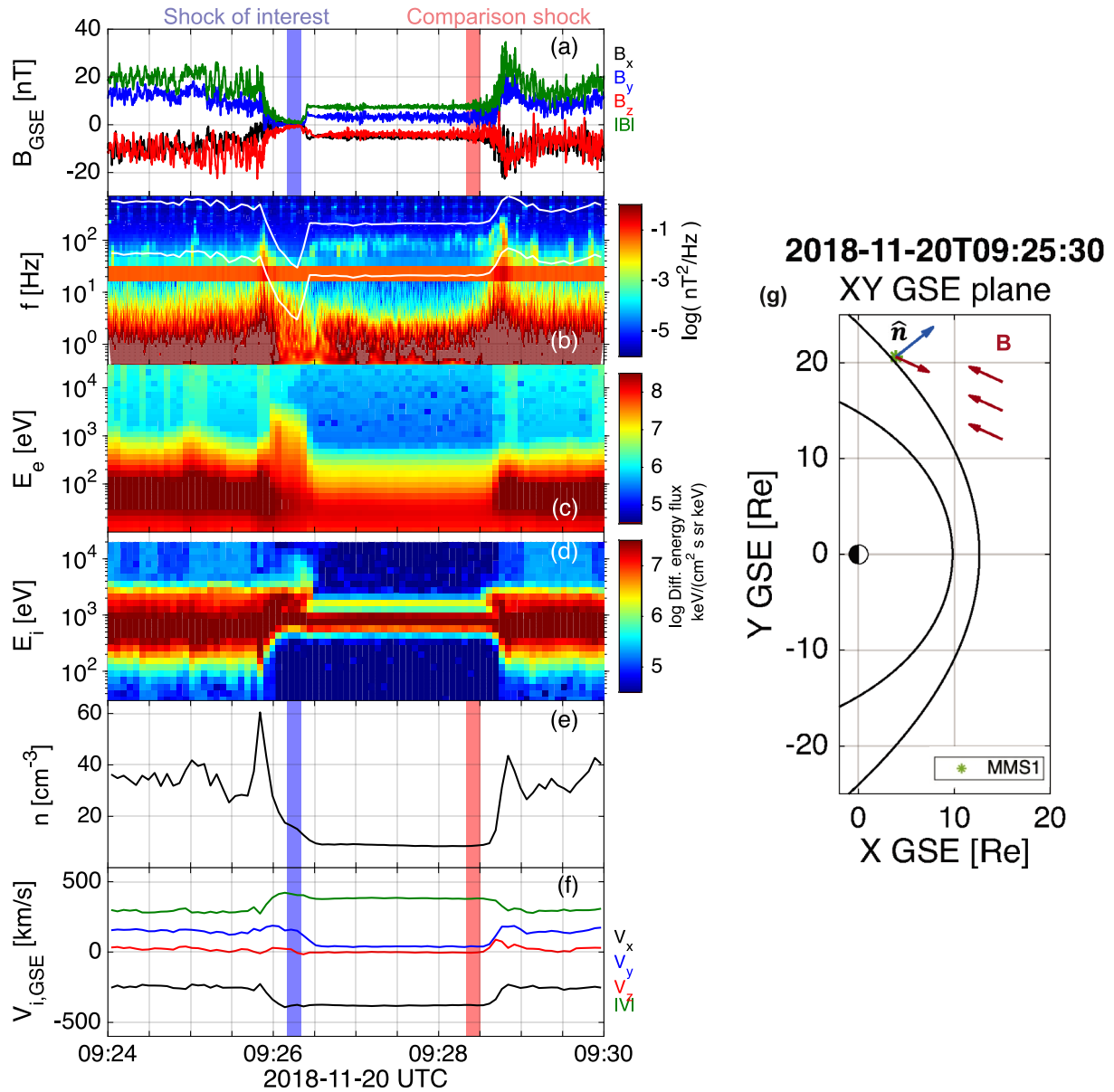
Figure 1. Data from MMS1 showing (a) magnetic field in Geocentric Solar Ecliptic (GSE) coordinates (b) magnetic field power spectral density where white lines indicate f_{ce} and $0.1 f_{ce}$. The prominent red band around 20 Hz is an instrumental artifact, and data from this frequency channel has been omitted in the analysis. Panel (c) omnidirectional electron energy flux (d) omnidirectional ion energy flux (e) particle density (f) ion bulk velocity in GSE coordinates and (g) showing bow shock and magnetopause models by Farris and Russell (1994) and Shue et al. (1998) respectively, along with Magnetospheric Multiscale location and upstream magnetic field direction. The blue-marked region indicates a 10-s time interval upstream of the shock of interest where the magnetic field strength reaches its minimum value (~1 nT). The red-marked region marks a 10-s time interval corresponding to a similar upstream distance away from the comparison shock as the blue region for the shock of interest.

unusually hard spectral index (p typically between -3 and -4 typically for Earth's bow shock (Gosling et al., 1989; Lindberg et al., 2024; Oka et al., 2006)) with an average of $p = -2.5$ throughout the whole EAR but reaches a value of $p = -2.3$ (black) as a maximum close to the shock.

Due to the non-steady upstream conditions, we determine a shock angle of $\theta_{Bn} \approx 78°$ for the shock of interest (shown in Figure 2) by using a shock normal of $\hat{n} = [0.78, 0.62, -0.08]_{GSE}$ obtained from the bow shock model from Farris and Russell (1994) and the location of MMS (see Figure 1g) while the upstream magnetic field was obtained from the L1 spacecraft. Using the density and velocity measurements upstream of the shock within the EAR, we determine an instantaneous shock velocity in the spacecraft frame of $V_{sh} = -70$ km/s based on the mass flux method described in Paschmann and Daly (2000). For the upstream magnetic wall observed by MMS,
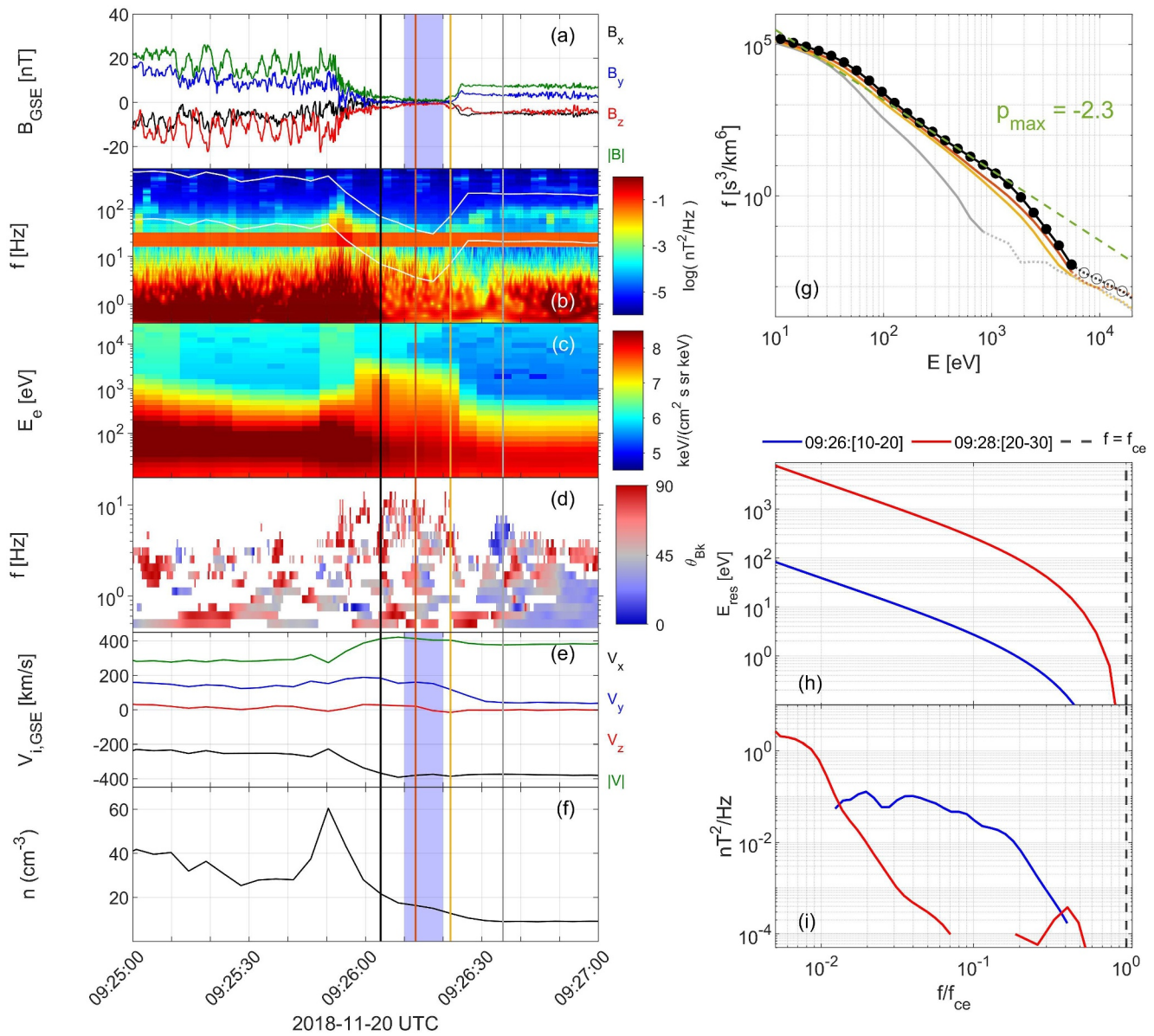
Figure 2. Zoomed-in view of the left shock crossing shown in Figure 1 showing (a) magnetic field in Geocentric Solar Ecliptic (GSE) coordinates (b) magnetic field power spectral density where white lines indicate f_{ce} and $0.1f_{ce}$. The prominent red band around 20 Hz is an instrumental artifact, and data from this frequency channel has been omitted in the analysis. Panel (c) electron differential flux (d) wave normal angle θ_{Bk} (e) ion bulk velocity in GSE coordinates (f) density. Panel (g) shows the electron distribution at four instances corresponding to the vertically black, brown, mustard yellow, and gray marked time instances in panels (a)–(f). The black curve with circles corresponds to where the hardest power-law slope is observed within the electron acceleration region, and the green dashed line is a power-law fit for the data between 200 and 1 keV. Panels (h) and (i) show the whistler cyclotron resonance energy and the average magnetic field wave power spectral density versus frequency for the blue-marked and red-marked regions in Figure 1.

we can estimate its relative motion using a timing analysis between the MMS1-4 spacecraft. We obtain an instantaneous speed in the spacecraft frame of $V_{\text{timing}} \approx 172$ km/s along the normal direction of the structure given by $\hat{n}_b = [-0.62, -0.78, -0.05]_{GSE}$.

2.2. Lagrange Point 1 (L1) Observations

To further investigate the origin of the magnetic boundary and the low magnetic field strength observed upstream of the primary shock, we study the upstream environment at the Lagrange point 1 (L1). Figure 3 shows the magnetic field measurements and locations of the L1 spacecraft DSCOVR (Burt & Smith, 2012), ACE (Stone
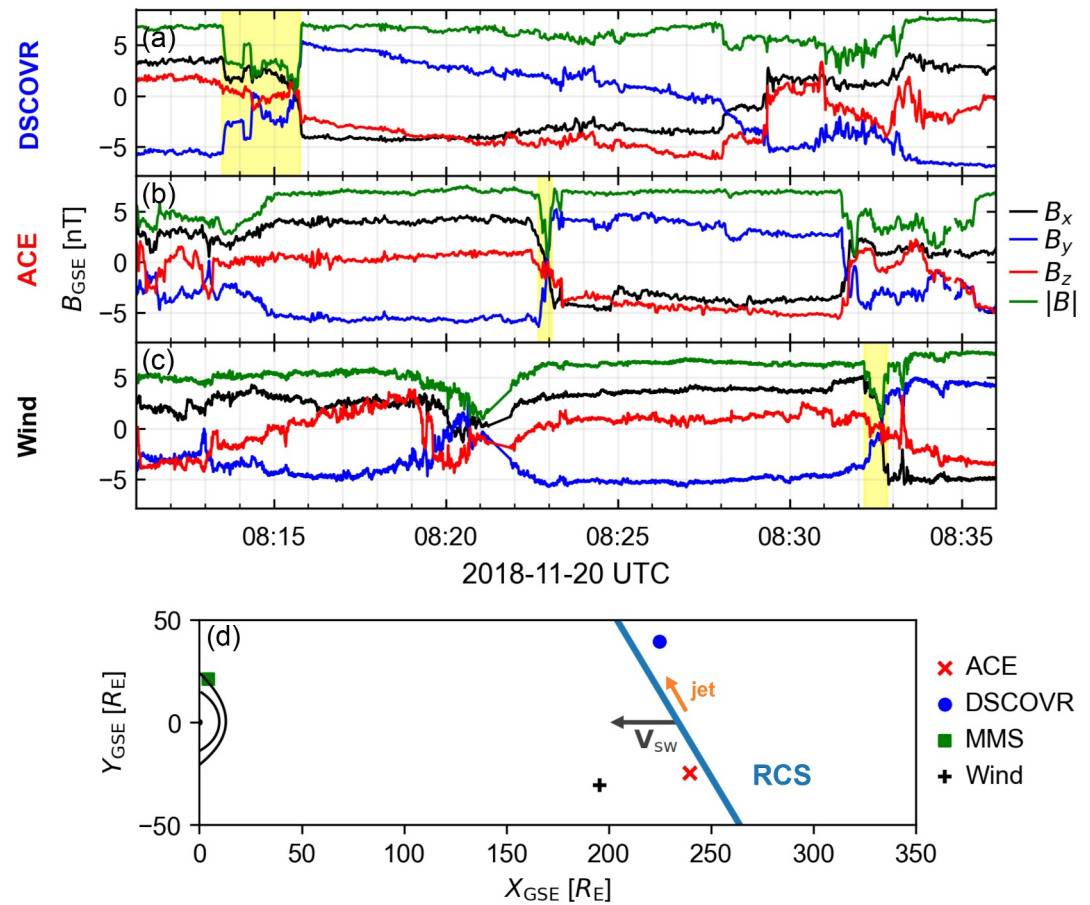
Figure 3. Lagrange point 1 magnetic field data from (a) DSCOVR, (b) ACE, and (c) Wind. Panel (d) shows spacecraft locations for the three above-mentioned spacecraft and Magnetospheric Multiscale. The thick blue line indicates the xy-plane orientation of the reconnecting current sheet highlighted in yellow in panels (a)–(c). The orange arrow indicates the reconnection exhaust jet direction measured by all three spacecraft.

et al., 1998), and Wind (Harten & Clark, 1995) approximately 1 hour before the event was observed by MMS (displayed in Figure 2). Around this time (08:00–09:00 UT), all L1 spacecraft observe three distinct magnetic depressions (Madanian et al., 2022). One of these magnetic depressions is highlighted in yellow for all three spacecraft in Figures 3a–3c and is identified as the structure later seen by MMS interacting with Earth's bow shock approximately 1 hour later at around 09:26:00 UT in Figures 1 and 2. The time lag between the L1 and MMS observation and a similar drop in magnetic field strength justifies the identification of the structure. Furthermore, a previous study by Madanian et al. (2022) investigated the interaction of Earth's bow shock with a solar wind RCS and its magnetic hole using MMS. That event takes place approximately 10 min after our event, around 09:33:00–09:38:00 UT as seen by MMS, and that structure can be seen at L1 between 08:28–08:33 UT in Figure 3a (DSCOVR) and between 08:32–08:35 UT in Figure 3b (ACE).

In Figure 4, we show zoomed-in Wind data around the magnetic depression highlighted in Figure 3c. Performing a minimum variance analysis on the magnetic field data selection highlighted in Figure 4a, suggests the magnetic depression is a RCS. From the minimum variance, we obtain the magnetic field and velocity in the LMN-coordinates, see Figures 4b and 4c. Crossing the structure, the LMN-magnetic field in Figure 4b shows a clear reversal in the maximum (L-coordinate) direction while the minimum (N-coordinate) stays very close to zero. The intermediate (M-coordinate) component is also very close to zero but shows a small bipolar signature.

At the same time, we calculate the LMN-velocity in the solar wind frame in Figure 4c. We observe an increase of roughly 30 km/s along the negative l-direction within the structure, which is comparable to the local solar wind Alfvén speed $v_{A,sw} \approx 40$ km/s, consistent with reconnection exhaust jets. This is further supported by the increase
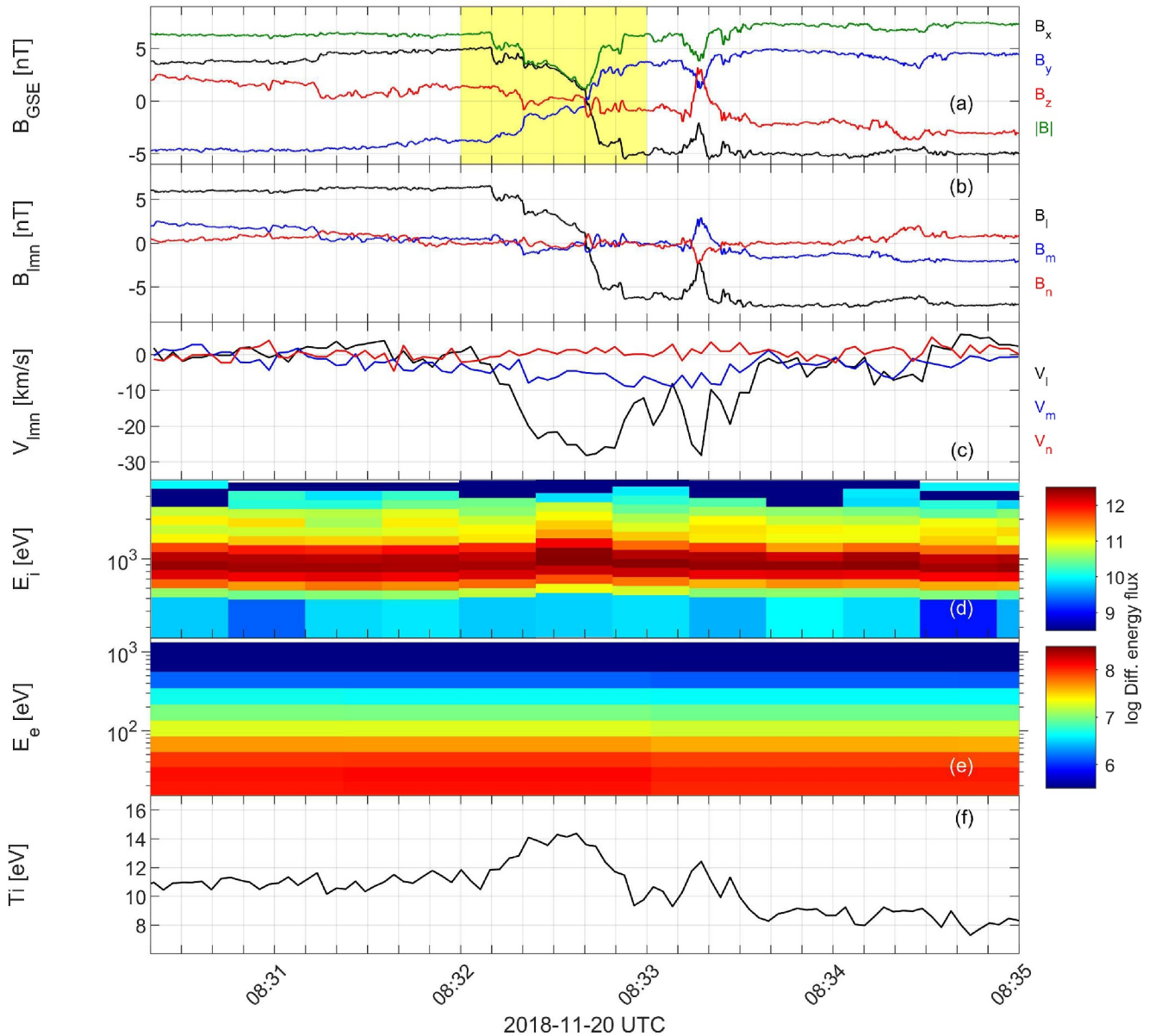
Figure 4. Minimum variance analysis using Wind data on the magnetic depression highlighted in Figure 3c. Panels show (a) magnetic field in Geocentric Solar Ecliptic coordinates and time interval used in the minimum variance analysis (yellow shaded region) (b) magnetic field in lmn-coordinates (c) ion velocity in LMN-coordinates in solar wind frame (d) ion differential energy flux (e) electron differential flux and (f) ion temperature.

in ion temperature in Figure 4f within the structure (Mistry et al., 2017). Note the absence of enhanced supra-thermal electron flux from Figure 4e. With the RCS seen by three different L1-spacecraft, we perform a timing analysis using Wind, ACE, and DSCOVR to obtain a global normal vector $\hat{n}_g = [0.77, 0.49, -0.41]_{GSE}$ of the RCS in the solar wind. Based on this normal, we can get a sense of the RCS orientation in the ecliptic plane. This is illustrated by the thick blue line in Figure 3d and is consistent with the order of appearance between the three L1 spacecraft in Figures 3a–3c. The observed transit times of the structure can be used to estimate the spatial size of the RCS at the different spacecraft locations. Assuming the structure convects with the solar wind speed, we can use that $\Delta x = V_{sw} \Delta t$. Using a solar wind speed $V_{sw} = 384$ km/s we get 7.2R_E (2 min) at DSCOVR, 1.2R_E (20 s) at ACE, and 2.4R_E (40 s) at Wind.
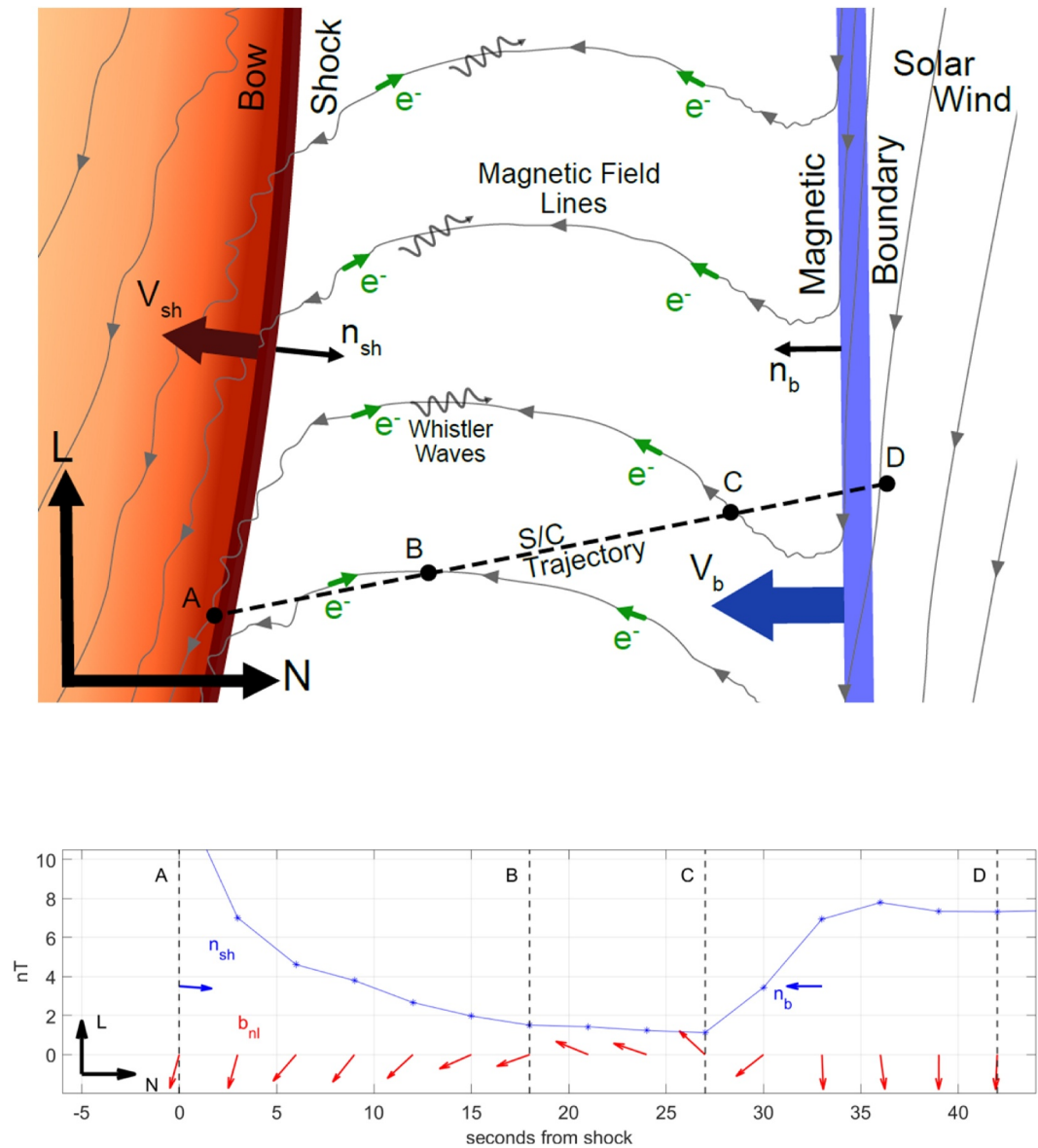
Figure 5. Illustration showing the magnetic topology between Earth's bow shock and the upstream magnetic boundary (current sheet edge) in the LN-plane of the LMN coordinate system of the magnetic boundary. The lower panel shows the magnetic field profile (blue curve) from the shock up to and across the upstream magnetic boundary. Red arrows indicate each data point's average magnetic field unit vector in the LN-plane.

3. Theory and Modeling

The observations outlined in the previous section suggests that MMS is observing Earth's bow shock (shock of interest) just as it is going through the solar wind RCS observed earlier upstream at L1 (highlighted in Figure 3) and the upstream magnetic boundary seen by MMS, corresponds to the right (later) edge of the same structure. Due to the very localized electron flux enhancement in the EAR, we suggest that the electrons are being energized via a transient Fermi acceleration process, in the low magnetic field region between the shock and the later edge of this RCS.

Figure 5a shows an illustration of the magnetic topology between the shock and the upstream magnetic boundary (current sheet edge) based on the MMS magnetic field data. The illustration is shown in the LN-plane where $N = \hat{n}_g$ is the global current sheet normal and L is the maximum coordinate obtained using a hybrid minimum analysis (Mistry et al., 2017) on the current sheet edge seen by MMS. The illustration shows the magnetic
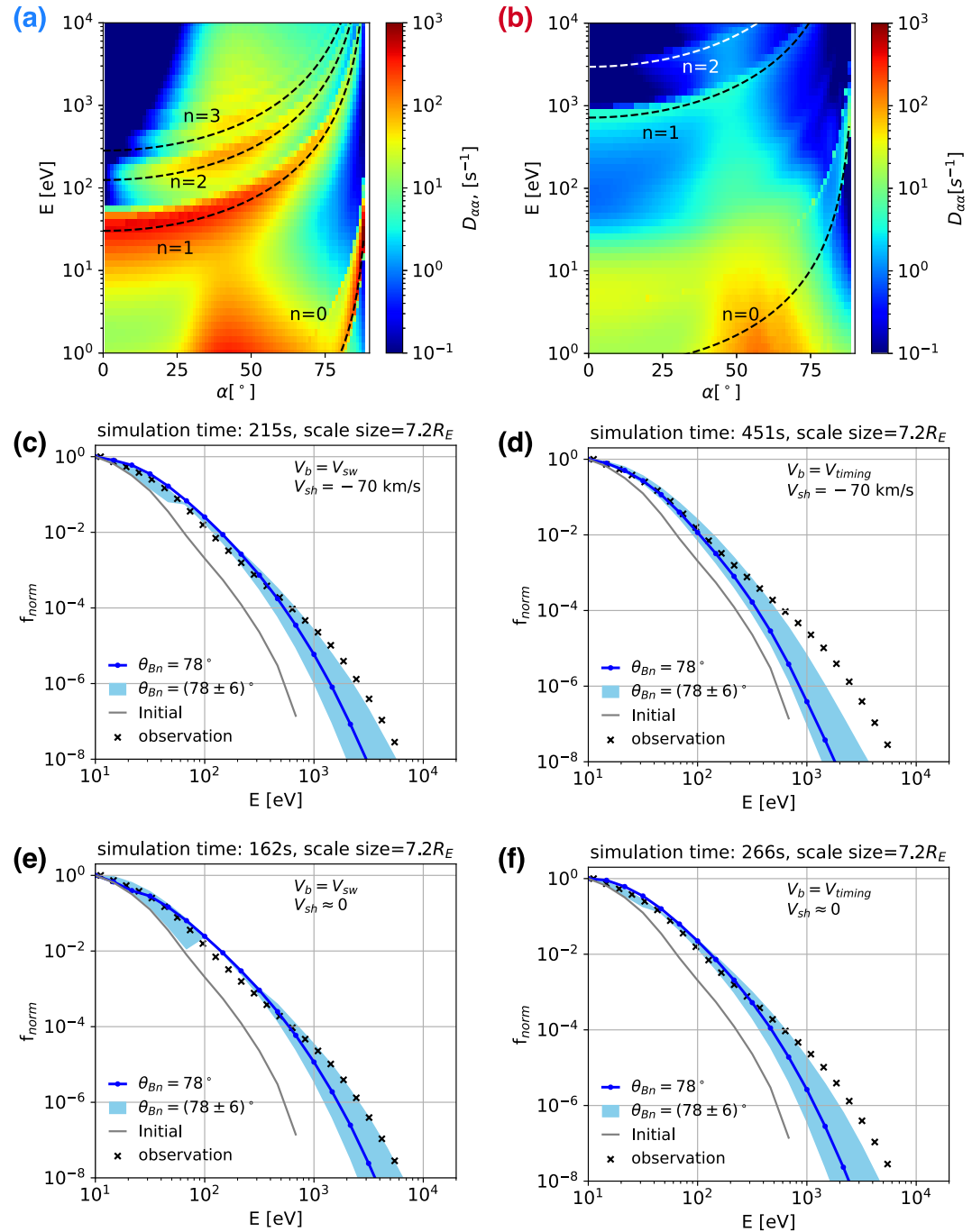
Figure 6. Comparing observations with a Fermi acceleration model from Shi et al. (2025). Panels (a) and (b) show bounce diffusion rates as a function of cyclotron resonance energy and electron pitch-angle α based on magnetic field power spectral density data between the lower hybrid frequency and $0.92f_{ce}$ from the blue (a) and red (b) regions highlighted in Figure 1b. The difference between them can be seen around the thermal energies 10–50 eV, where the blue case shows a much higher diffusion rate than the red case, indicating that the waves are in resonance with the thermal and suprathermal population. Dashed lines show the resonance curve with different n values. Panels (c)–(f) show our Fermi acceleration model for four different setups of boundary and shock velocities V_b and V_{sh} whose value in turn determines the total simulation time. The gray curve indicates the initial (solar wind) distribution obtained from the time instant marked with a vertical gray line in Figure 2. Black crosses mark the average distribution function over the whole electron acceleration region (09:26:00–09:26:20 UT) measured by Magnetospheric Multiscale. Blue curve corresponds to the model output using a measured shock angle of $\theta_{Bn} = 78°$ with light blue shade indicating $\pm6°$ deviation.

connectivity between the shock and the magnetic boundary, and a hypothetical spacecraft trajectory consistent with the measured magnetic field directions is also shown in Figure 5b.

Further evidence is the unusually hard spectral index (slope), $p = -2.3$, observed for energies above 100 eV, compared to the typical values found at Earth's bow shock (between -3 and -4). The spectral index relates to the probability of a particle escaping an acceleration mechanism (Longair, 1981), where a harder index means better confinement, for example in first-order Fermi acceleration, the predicted spectral index is determined by the ratio of up-to downstream bulk velocity or density compression $r = V_u/V_d = n_d/n_u$ according to (Oka et al., 2018)

$$p = -\frac{3r}{2(r-1)}. \tag{1}$$

The density compression ratio for the shock of interest in Figure 2 is $r = 3.5$: using this value in Equation 1 yields a theoretical spectral index of $p = -2.1$, which is very close to the observed one of $p = -2.3$.

Another key component in the presented Fermi acceleration framework and many other electron acceleration mechanisms is the presence of potential wave modes able to pitch-angle scatter electrons to keep them in the acceleration process longer. The high intensity of magnetic field wave power in the EAR (see Figure 2b) is most likely due to the low background magnetic field strength inside the RCS. Whistler waves are commonly found in the foot region upstream of collisionless bow shocks (Lalti et al., 2022; Oka et al., 2006; Sulaiman et al., 2017). They are typically known to be mostly low frequency $(<0.1f_{ce})$, oblique but close to parallel propagating (Lalti et al., 2022), and able to pitch-angle scatter electrons with energies above 1 keV (Amano et al., 2020). However, as the RCS sweeps across Earth's bow shock, the whistler waves in front of the shock find themselves in a much lower background magnetic field ($B \sim 1$–2 nT), which in turn corresponds to lower cyclotron frequencies f_{ce} and f_{ci}. Moreover, we estimate the wave amplitude to background magnetic field ratio in the EAR to be $\delta B/B_0 = \sigma_B/\langle B \rangle \approx 0.3$ where σ_B is the standard deviation and angle brackets denote the average (Perri & Zimbardo, 2012). This indicates that there are waves with amplitudes in the same order as the background magnetic field and very strong pitch angle scattering is present.

We can calculate the cyclotron resonance energy of non-relativistic electrons E_{res}, assuming a cold whistler dispersion relation (Swanson, 2020)

$$\left(\frac{ck}{\omega}\right)^2 = \frac{\omega_{pe}^2}{(\Omega_{ce} - \omega)\omega} - \frac{\omega_{pi}^2}{(\Omega_{ci} + \omega)\omega}, \tag{2}$$

and a cyclotron resonance condition (Katou & Amano, 2019)

$$\omega - kv\mu = \Omega_{ce}, \tag{3}$$

where $\omega = 2\pi f$ is the (angular) frequency, k the wavenumber, v the electron velocity, $\mu = \cos \alpha$ is the cosine of an electrons pitch angle α, Ω_{ce} and Ω_{ci} the electron and ion (angular) cyclotron frequencies, and Ω_{pe} and Ω_{pi} the electron and ion (angular) plasma frequencies. Moreover, we correct the frequency for the Doppler shift using

$$\omega \rightarrow \omega - k\hat{\mathbf{b}} \cdot \langle \mathbf{V}_i \rangle, \tag{4}$$

where $\langle \mathbf{V}_i \rangle$ is the average ion bulk velocity within the relevant time interval, and assuming the whistler waves are parallel propagating. Note that the whistler waves in our case are not completely parallel propagating. As seen from Figure 2d, they have an electrostatic component in the EAR. We use the parallel propagation assumption for simplifying the analytical treatment to illustrate the change in wave-particle interaction as the background magnetic field change.

The calculated resonance energy $E_{res} = m_e v^2/2$ for a selected pitch angle of 45° can be seen in Figure 2h as a function of frequency for the two (red and blue) highlighted time intervals in Figure 1, while Figure 2i shows the average magnetic field power spectral density for the same time intervals. The red curves in Figures 2h and 2i correspond to a typical shock crossing where most wave power is delivered at low frequencies corresponding to electron resonant energies above 1 keV. However, studying the blue curves in Figures 2h and 2i, which

corresponds to our shock of interest, we see several orders of magnitude higher wave power between 0.02 and 0.2 f_{ce} corresponding to electron resonance energies in the thermal range of 1–30 eV. Hence, the drop in magnetic field magnitude enables the whistler waves to directly pitch angle scatter electrons in the broad thermal energy range, enhancing their confinement between the shock and the approaching upstream magnetic boundary (current sheet edge).

3.1. Fermi Acceleration Model

To further investigate our Fermi acceleration hypothesis, we set up a Fermi acceleration model that includes the electron pitch-angle scattering by whistler-mode waves. In this model, we consider that the shock and the upstream magnetic boundary form a magnetic bottle structure (as shown in Figure 5a) that can trap electrons. During the bouncing motion inside the magnetic bottle, electrons can experience Fermi acceleration and can be scattered by whistler-mode waves. The observed whistler-mode waves are obliquely propagating as inferred from Figure 2d. We use the method proposed by Glauert and Horne (2005) to calculate the pitch angle diffusion coefficient $D_{\alpha\alpha}$.

$$
\begin{aligned}
D_{\alpha\alpha} &= \sum_{n=n_l}^{n_h} \int_{X_{min}}^{X_{max}} D_{\alpha\alpha}^{(nX)} X dX \\
D_{\alpha\alpha}^{(nX)} &= \sum_i \frac{e^2 \omega_i^2}{4\pi(1+X^2)} \left[\frac{n\Omega_{ce}/\omega_i - \sin^2\alpha}{\cos^2\alpha} \right]^2 F(\omega_i)\, g(X)\, \mathcal{N}(n,k,\omega_i)
\end{aligned}
\tag{5}
$$

where $X = \tan\theta_{Bk}$ with θ_{Bk} being the wave normal angle, $g(X)$ is the distribution of the wave normal angle, $F(\omega)$ is the wave power spectrum, and $\mathcal{N}$ is a function determined by wave dispersion (detailed derivations can be found in Glauert & Horne, 2005). The resonance condition is $\omega - k_\parallel v_\parallel = n\Omega_{ce}$, where $n = 1$ corresponds to the cyclotron resonance with electrons, $n = 0$ corresponds to the Landau resonance, and $|n| > 1$ denotes higher harmonic cyclotron resonances. Only the fundamental (first-order $n = 1$) cyclotron resonance exists for parallel-propagating whistler-mode waves. However, for oblique-propagating waves, zero- and high-order resonances are also allowed. Therefore, the oblique whistler-mode waves can resonate with electrons across a wider energy range compared to parallel waves (e.g., Artemyev et al., 2016). For a given energy, resonance number n, and wave normal angle θ_{Bk}, there may be more than one resonant frequency (ω_n) (Albert, 1999; Glauert & Horne, 2005). The sum of the contributions from all resonances determines the total effect of pitch-angle scattering.

The distribution of $F(\omega)$ with frequencies between lower-hybrid frequency and electron cyclotron frequency can be obtained from the observations, and we assume the wave normal angle follows a Gaussian distribution as $g(X) = \exp(-(X - X_m)^2/X_w^2)$ where X_m and X_w are the average and width values obtained from observations ($\theta_{Bk} = 47° \pm 22°$ from the blue shaded region in Figure 2). Figures 6a and 6b show the diffusion coefficients calculated for the plasma and wave parameters associated with the blue (EAR) and red regions (comparison shock) in Figure 1, respectively. The main difference between them can be seen around the thermal energies 10–50 eV, where the blue case shows a much higher diffusion rate than the red case, indicating that the waves are in resonance with the thermal and suprathermal population. Hence, the whistler-mode waves in the EAR are more effective in scattering thermal and suprathermal electrons compared to the typical (red) case.

To incorporate the pitch angle scattering effects in the electron bouncing motion, we then calculate the bounce-averaged pitch angle diffusion coefficient $\langle D_{\alpha_0\alpha_0} \rangle$ in the EAR as $\langle D_{\alpha_0\alpha_0} \rangle = (1/\tau_b)\int_{\tau_b} D_{\alpha\alpha}(\partial\alpha_0/\partial\alpha)^2 dt$, where α_0 is the pitch angle value at the minimum magnetic field strength location and τ_b is the time period of electron bouncing motion between the shock and upstream boundary, and L is the spatial scale of the EAR. In the simulation, the magnetic moment is conserved around the boundaries (shock and upstream current sheet edge) where the reflection occurs, and the wave-particle interactions can pitch angle scatter electrons and break the conservation of magnetic moment in the middle of the simulation box (EAR). Therefore, we include this change into evaluation of the bounce period within a simple estimate: $\tau_b \approx \int ds/v_\parallel(s) = \int_L ds/(2V) + \int_{L'} ds/(2V')$, where L, V are the spatial scale and parallel velocity before pitch-angle change due to wave-particle interaction and L' and V' are the spatial scale and parallel velocity after half of a bounce period estimated using L and V. Note that τ_b now serves as a first-order approximation of the full bounce period, combining one half of the integral with the magnetic moment conserved at the start of the bounce and the other half evaluated after pitch-angle scattering.

We numerically simulate electron dynamics affected by a combination of electron scattering and acceleration to reproduce the observed energy spectrum (see details of numerical scheme in Shi et al., 2025). The elementary time-step in the model is the electron's bounce period. The initial electron energy distribution is obtained from the solar wind observations (gray curves in Figures 2g and 6c–6f), and we assume a uniform initial pitch angle distribution, similar to what is observed in the solar wind outside of the EAR (gray line/curve in Figure 2). The initial bouncing spatial scale is L. Assuming the width of the current sheet does not change drastically between L1 and Earth's bow shock, we set $L = 7.2\ R_{\rm E}$, as measured by DSCOVR, because of the best alignment with MMS out of the three L1 spacecraft (See Figure 3d). As the simulation progresses, L shrinks as the shock and upstream boundary move toward each other, affecting the electron bounce time τ_b. During each bounce, electrons experience pitch-angle scattering caused by whistler-mode waves and Fermi acceleration due to the movement of the shock and upstream boundary. The pitch angle change due to scattering is $\Delta\alpha_0 = W\sqrt{\langle D_{\alpha_0\alpha_0}(E,\alpha)\rangle\tau_b}$ where W is a random number from the normal Gaussian probability distribution with a zero mean value and unity dispersion. Note that the energy change due to wave-particle interactions is negligible, and therefore, the pitch-angle change can be directly recalculated into changes of parallel and perpendicular energy components. The parallel velocity change due to Fermi acceleration is $\Delta v_{\|,\rm Fermi} = 2V_{\rm n}/\cos\theta_{Bn}$ where $V_{\rm n} = V_{\rm b} - V_{\rm sh}$. At the end of each bounce period, we determine whether the electron's pitch angle is within the loss cone ($22°$ at the upstream boundary and $12°$ at the shock). If the pitch angle is within the loss cone, the electron is excluded from the simulation and replaced by a new electron randomly selected from the initial distribution.

The simulation results for an initial scale size of $L = 7.2R_{\rm E}$ and four different setups of simulation time, and boundary approaching velocities $V_{\rm n}$ (combinations of $V_{\rm sh}$ and $V_{\rm b}$) are shown in Figures 6c–6f. The four combinations of boundary approaching velocity are constructed assuming a magnetic boundary velocity $V_{\rm b} = \mathbf{V}_{\rm sw}\cdot\mathbf{n}_{\rm b} = 238$ km/s and $V_{\rm b} = V_{\rm timing} = 172$ km/s along the boundary normal $n_{\rm b}$ and an instantaneous shock velocity of $V_{\rm sh} = -70$ km/s and $V_{\rm sh} = 0$ in the shock frame.

For each set of simulation runs, we simulate 10^7 electrons and trace their energies and pitch angles. The blue curves represent the normalized electron spectra obtained from simulations with $\theta_{Bn} = 78°$, and the blue shaded regions indicate the results for $\theta_{Bn} \pm 6°$. Black crosses show the normalized averaged spectrum measured by MMS within the whole EAR.

The results demonstrate good agreement between the simulations and observations for reasonable settings of parameters, particularly for the case where the boundary velocity $V_{\rm b}$ is equal to the solar wind speed, as illustrated in Figure 6e.

4. Discussion

The Fermi acceleration model fits the data best for a magnetic boundary speed of the solar wind speed and an (on average) assumed stationary shock ($V_{\rm sh} = 0$), see Figure 6e. This assumption is reasonable, considering the scale size of the structure being estimated to $7.2R_{\rm E}$. The time for such a large structure to cross the bow shock is in the order of minutes, and during that time, the motion of the bow shock would likely average to zero. Hence, a constant shock speed of around -70 km/s for such a long time seems quite unlikely. Due to the slight inconsistency between the boundary speed from the timing analysis performed on the structure at L1 (238 km/s) and at MMS (172 km/s), we decided to run the model using both of those speeds. Note that the speed determined using timing analysis at MMS is slightly less than that of the structure convecting with the solar wind speed (as suggested by the L1 observations). This suggests that the current sheet might either be expanding in the solar wind frame or slowing down as it encounters and interacts with Earth's bow shock. However, the difference is not substantial and may also be due to the limitations of the timing method used to determine the speed at MMS.

All four sets of parameters used in Figures 6c–6f produce a too-low energy cutoff. However, taking the uncertainty in shock angle θ_{Bn} into account shows that the model can reach the higher energies observed by MMS in the EAR. Also note that, for model runs with a higher cut-off (see e.g. upper edge of blue shaded region in Figure 6e), the spectral slope of the model matches well with the observed $\langle p\rangle \approx -2.5$ within the EAR. Considering that this is a simplified model, with limitations such as the use of a one-dimensional magnetic field model and the exclusion of feedback from accelerated electrons on the waves, we find the overall agreement to be very good. Additionally, the wave amplitudes within the EAR are shown to be in the same order as the background magnetic field, $\delta B/B \approx 0.3$. This is beyond the quasi-linear theory assumption made in the model, and nonlinear effects

would potentially result in a higher pitch angle and energy diffusion rate, a few times larger than the quasi-linear theory prediction.

Unfortunately, there was no MMS burst data available at the presented event. Hence, the data shown in this paper is fast-mode data. For the plasma data, this mainly affects the high energy channels via unwanted data compression (Barrie et al., 2017), which acts as an elevated noise level. Therefore, data points within this noise level should not be trusted and have not been considered (see shaded and dotted lines in Figure 2g).

The work of this paper showcases a mechanism through which thermal electrons can be accelerated to supra-thermal energies at Earth's bow shock via the interaction of a reconnecting solar wind current sheet. Note that the Wind data showed little to no energetic electrons at L1, meaning that the amount of suprathermal electrons observed in the EAR with MMS is accelerated locally between the bow shock and the upstream magnetic boundary. Although the highest energy reached by the electrons (1–5 keV) are quite modest compared to what has been previously shown at Earth's bow shock (Amano et al., 2020; Lindberg et al., 2023, 2024; Raptis, Lalti, et al., 2025; Raptis, Lindberg, et al., 2025; Wilson et al., 2016), a power-law spectral index this hard ($p = -2.3$) is rarely observed at Earth's bow shock which typically lies between -3 and -4 (Lindberg et al., 2024; Oka et al., 2006). As mentioned above, the spectral index relates to the probability of particles staying in an accel-eration process. The much harder spectral index therefore shows that this process is more efficient in confining the electrons in the acceleration mechanism compared to the standard acceleration mechanisms typically found at Earth's bow shock, such as SDA (Wu, 1984) and SSDA (Amano & Hoshino, 2022). We identify two main reasons for this. The first is the presence of an approaching upstream magnetic wall, which can adiabatically reflect upstream escaping electrons back into the EAR. Secondly, the temporary decrease in background magnetic field strength (or increase in the f_{pe}/f_{ce} ratio) inside the current sheet enables upstream whistler waves to interact with thermal-energy electrons. The drop in cyclotron frequencies changes the whistler-mode wave's dispersion rela-tion, driving the originally low-frequency waves toward higher frequencies and a more oblique propagation. Moreover, in the case of the EAR, whistler-mode waves can interact with higher-energy electrons primarily because they exhibit high intensity at both middle and low frequencies. Additionally, the increased wave obliqueness helps broaden the resonance energy range, further enhancing the interactions.

A crucial component of our study is the low magnetic field strength within the current sheet, which creates ideal electron confinement conditions as it convects across the shock. The mechanism described in this study should hold for any solar wind magnetic depression, such as current sheets, but also for example solar wind magnetic holes (Sperveslage et al., 2000; J. Turner et al., 1977) given their magnetic topology would allow for particles to be trapped similarly to our illustration in Figure 5. Recent studies show that magnetic holes are frequently generated in the solar wind (Yu et al., 2021) and that they can cross the bow shock and enter Earth's magneto-sheath (Karlsson et al., 2022). However, there is still no direct observation of the exact moment a magnetic hole crosses the bow shock. Its implications on the particle dynamics are left to speculation and future observations.

One of the still open questions regarding the most common electron acceleration mechanism (SSDA) to explain the electron injection problem is the lack of sufficient pitch angle scattering for electrons below 1 keV (Amano & Hoshino, 2022). While ongoing work suggests the solution to be electrostatic waves (Kamaletdinov et al., 2022; Vasko et al., 2018), for the case study presented in this paper, electrostatic waves are not essential since the whistler waves can sufficiently scatter the thermal electrons over a broad range of energies. However, a crucial difference between the proposed Fermi mechanism outlined in this work and common electron acceleration mechanisms at collisionless shocks is the limited time (transient-type) the shock stays within the current sheet. This limits the number of bounces the electrons can do between the shock and the upstream current sheet edge and explains the modest ∼1 keV energies reached by the process. Similar acceleration mechanisms have recently been studied in Shi et al. (2025), Raptis, Lalti, et al. (2025), and Raptis, Lindberg, et al. (2025), where mildly relativistic electrons have been observed around upstream foreshock transients. Shi et al. (2025) suggests that electrons can gain relativistic energies through repeated reflections between the Earth's bow shock and such transient phe-nomena, more frequently observed upstream of quasi-parallel shocks. In contrast, Raptis, Lalti et al. (2025) and Raptis, Lindberg, et al. (2025) showed in situ evidence of relativistic electrons getting energized within and in the vicinity of such transients. Together with these recent works, our study highlights the impact that upstream solar wind transients structures can have on electron acceleration when interacting with planetary bow shocks and the different ways the interactions can reinforce the acceleration.

Data Availability Statement

The MMS data used in this paper were obtained from the Fast Plasma Investigation (FPI) (Pollock et al., 2016), Flux-Gate Magnetometer (FGM) (Russell et al., 2016), and Search Coil Magnetometer (SCM) (Le Contel et al., 2016). All data can be obtained from the MMS Science Data Center (Larsen et al., 2016). The DSCOVR, ACE, and Wind data were obtained from the NASA CDA Web available at https://cdaweb.gsfc.nasa.gov/. Data analysis was performed using the IRFU-Matlab analysis package available at (Nilsson, 2022). The observational data and Julia code used to calculate the pitch angle diffusion coefficients can be found here https://zenodo.org/records/13910524 (Shi, 2024).

References

Albert, J. M. (1999). Analysis of quasi-linear diffusion coefficients. *Journal of Geophysical Research*, *104*(A2), 2429–2441. https://doi.org/10.1029/1998JA900113

Amano, T., & Hoshino, M. (2022). Theory of electron injection at oblique shock of finite thickness. *The Astrophysical Journal*, *927*(1), 132. https://doi.org/10.3847/1538-4357/ac4f49

Amano, T., Katou, T., Kitamura, N., Oka, M., Matsumoto, Y., Hoshino, M., et al. (2020). Observational evidence for stochastic shock drift acceleration of electrons at the Earth's bow shock. *Physical Review Letters*, *124*(6), 065101. https://doi.org/10.1103/PhysRevLett.124.065101

Artemyev, A., Agapitov, O., Mourenas, D., Krasnoselskikh, V., Shastun, V., & Mozer, F. (2016). Oblique whistler-mode waves in the Earth's inner magnetosphere: Energy distribution, origins, and role in radiation belt dynamics. *Space Science Reviews*, *200*(1–4), 261–355. https://doi.org/10.1007/s11214-016-0252-5

Ball, L., & Melrose, D. (2001). Shock drift acceleration of electrons. *Publications of the Astronomical Society of Australia*, *18*(4), 361–373. https://doi.org/10.1071/as01047

Bamba, A., Yamazaki, R., & Hiraga, J. S. (2005). Chandra observations of galactic supernova remnant vela jr.: A new sample of thin filaments emitting synchrotron X-Rays. *The Astrophysical Journal*, *632*(1), 294–301. https://doi.org/10.1086/432711

Barrie, A. C., Smith, S. E., Dorelli, J. C., Gershman, D. J., Yeh, P., Schiff, C., & Avanov, L. A. (2017). Performance of a space-based wavelet compressor for plasma count data on the MMS fast plasma investigation. *Journal of Geophysical Research: Space Physics*, *122*(1), 765–779. https://doi.org/10.1002/2016JA022645

Blandford, R., & Eichler, D. (1987). Particle acceleration at astrophysical shocks: A theory of cosmic ray origin. *Physics Reports*, *154*(1), 1–75. https://doi.org/10.1016/0370-1573(87)90134-7

Burch, J. L., Moore, T. E., Torbert, R. B., & Giles, B. L. (2016). Magnetospheric multiscale overview and science objectives. *Space Science Reviews*, *199*(1), 5–21. https://doi.org/10.1007/s11214-015-0164-9

Burt, J., & Smith, B. (2012). Deep space climate observatory: The DSCOVR mission. In *2012 IEEE aerospace conference* (pp. 1–13). https://doi.org/10.1109/AERO.2012.6187025

Bykov, A., & Treumann, R. (2011). Fundamentals of collisionless shocks for astrophysical application, 2. Relativistic shocks. *Astronomy and Astrophysics Review*, *19*, 1–67. https://doi.org/10.1007/s00159-011-0042-8

Drury, L. O. (1983). An introduction to the theory of diffusive shock acceleration of energetic particles in tenuous plasmas. *Reports on Progress in Physics*, *46*(8), 973–1027. https://doi.org/10.1088/0034-4885/46/8/002

Farris, M., & Russell, C. (1994). Determining the standoff distance of the bow shock: Mach number dependence and use of models. *Journal of Geophysical Research*, *99*(A9), 17681–17689. https://doi.org/10.1029/94ja01020

Giacalone, J. (2005). Particle acceleration at shocks moving through an irregular magnetic field. *The Astrophysical Journal*, *624*(2), 765–772. https://doi.org/10.1086/429265

Glauert, S. A., & Horne, R. B. (2005). Calculation of pitch angle and energy diffusion coefficients with the PADIE code. *Journal of Geophysical Research: Space Physics*, *110*(A4), A04206. https://doi.org/10.1029/2004JA010851

Goodrich, C. C., & Scudder, J. D. (1984). The adiabatic energy change of plasma electrons and the frame dependence of the cross-shock potential at collisionless magnetosonic shock waves. *Journal of Geophysical Research*, *89*(A8), 6654–6662. https://doi.org/10.1029/JA089iA08p06654

Gosling, J. T., Thomsen, M. F., Bame, S. J., & Russell, C. T. (1989). Suprathermal electrons at Earth's bow shock. *Journal of Geophysical Research*, *94*(A8), 10011–10025. https://doi.org/10.1029/JA094iA08p10011

Harten, R., & Clark, K. (1995). The design features of the GGS wind and polar spacecraft. *Space Science Reviews*, *71*(1–4), 23–40. https://doi.org/10.1007/BF00751324

Johlander, A., Battarbee, M., Vaivads, A., Turc, L., Pfau-Kempf, Y., Ganse, U., et al. (2021). Ion acceleration efficiency at the Earth's bow shock: Observations and simulation results. *The Astrophysical Journal*, *914*(2), 82. https://doi.org/10.3847/1538-4357/abfafc

Kamaletdinov, S. R., Vasko, I. Y., Artemyev, A. V., Wang, R., & Mozer, F. S. (2022). Quantifying electron scattering by electrostatic solitary waves in the Earth's bow shock. *Physics of Plasmas*, *29*(8), 082301. https://doi.org/10.1063/5.0097611

Karlsson, T., Trollvik, H., Raptis, S., Nilsson, H., & Madanian, H. (2022). Solar wind magnetic holes can cross the bow shock and enter the magnetosheath. In *Annales Geophysicae* (Vol. 40(6), pp. 687–699). https://doi.org/10.5194/angeo-40-687-2022

Katou, T., & Amano, T. (2019). Theory of stochastic shock drift acceleration for electrons in the shock transition region. *The Astrophysical Journal*, *874*(2), 119. https://doi.org/10.3847/1538-4357/ab0d8a

King, J. H., & Papitashvili, N. E. (2005). Solar wind spatial scales in and comparisons of hourly wind and ACE plasma and magnetic field data. *Journal of Geophysical Research*, *110*(A2), A02104. https://doi.org/10.1029/2004ja010649

Koyama, K., Petre, R., Gotthelf, E. V., Hwang, U., Matsuura, M., Ozaki, M., & Holt, S. S. (1995). Evidence for shock acceleration of high-energy electrons in the supernova remnant SN1006. *Nature*, *378*(6554), 255–258. https://doi.org/10.1038/378255a0

Lalti, A., Khotyaintsev, Y. V., Graham, D. B., Vaivads, A., Steinvall, K., & Russell, C. T. (2022). Whistler waves in the foot of quasi-perpendicular supercritical shocks. *Journal of Geophysical Research: Space Physics*, *127*(5), e2021JA029969. https://doi.org/10.1029/2021JA029969

Larsen, K. W., Pankratz, C. K., Kokkonen, K., Putnam, B., Schafer, C., Baker, D. N., & Burch, J. (2016). The magnetospheric multiscale (MMS) science data center [Dataset]. *AGU Fall Meeting Abstracts*. https://lasp.colorado.edu/mms/sdc/public/datasets/

Le Contel, O., Leroy, P., Roux, A., Coillot, C., Alison, D., Bouabdellah, A., et al. (2016). The search-coil magnetometer for MMS. *Space Science Reviews*, *199*(1), 257–282. https://doi.org/10.1007/s11214-014-0096-9

Levinson, A. (1992). Electron injection in collisionless shocks. *Astrophysical Journal Part 1*, *401*, 73–80. https://doi.org/10.1086/172039

Lindberg, M., Vaivads, A., Amano, T., Raptis, S., & Joshi, S. (2024). Electron acceleration at Earth's bow shock due to stochastic shock drift acceleration. *Geophysical Research Letters*, *51*(5), e2023GL106612. https://doi.org/10.1029/2023GL106612

Lindberg, M., Vaivads, A., Raptis, S., & Karlsson, T. (2023). MMS observation of two-step electron acceleration at earth's bow shock. *Geophysical Research Letters*, *50*(16), e2023GL104714. https://doi.org/10.1029/2023GL104714

Liu, T. Z., Angelopoulos, V., & Lu, S. (2019). Relativistic electrons generated at earth's quasi-parallel bow shock. *Science Advances*, *5*(7), eaaw1368. https://doi.org/10.1126/sciadv.aaw1368

Liu, T. Z., Lu, S., Angelopoulos, V., Hietala, H., & Wilson, L. B. III. (2017). Fermi acceleration of electrons inside foreshock transient cores. *Journal of Geophysical Research: Space Physics*, *122*(9), 9248–9263. https://doi.org/10.1002/2017ja024480

Longair, M. S. (1981). High energy astrophysics. An informal introduction for students of physics and astronomy.

Madanian, H., Liu, T. Z., Phan, T. D., Trattner, K. J., Karlsson, T., & Liemohn, M. W. (2022). Asymmetric interaction of a solar wind reconnecting current sheet and its magnetic hole with Earth's bow shock and magnetopause. *Journal of Geophysical Research: Space Physics*, *127*(4), e2021JA030079. https://doi.org/10.1029/2021JA030079

Mistry, R., Eastwood, J., Phan, T., & Hietala, H. (2017). Statistical properties of solar wind reconnection exhausts. *Journal of Geophysical Research: Space Physics*, *122*(6), 5895–5909. https://doi.org/10.1002/2017ja024032

Nilsson, T. (2022). GitHub.com. (version 1.16.3) [Software]. https://github.com/irfu/irfu-matlab/

Oka, M., Birn, J., Battaglia, M., Chaston, C. C., Hatch, S. M., Livadiotis, G., et al. (2018). Electron power-law spectra in solar and space plasmas. *Space Science Reviews*, *214*(5), 82. https://doi.org/10.1007/s11214-018-0515-4

Oka, M., Terasawa, T., Seki, Y., Fujimoto, M., Kasaba, Y., Kojima, H., et al. (2006). Whistler critical mach number and electron acceleration at the bow shock: Geotail observation. *Geophysical Research Letters*, *33*(24), L24104. https://doi.org/10.1029/2006GL028156

Paschmann, G., & Daly, P. W. (2000). Analysis methods for multi-spacecraft data.

Perri, S., Bykov, A., Fahr, H., Fichtner, H., & Giacalone, J. (2022). Recent developments in particle acceleration at shocks: Theory and observations. *Space Science Reviews*, *218*(4), 26. https://doi.org/10.1007/s11214-022-00892-5

Perri, S., & Zimbardo, G. (2012). Magnetic variances and pitch-angle scattering times upstream of interplanetary shocks. *The Astrophysical Journal*, *754*(1), 8. https://doi.org/10.1088/0004-637X/754/1/8

Pollock, C., Moore, T., Jacques, A., Burch, J., Gliese, U., Saito, Y., et al. (2016). Fast plasma investigation for magnetospheric multiscale. *Space Science Reviews*, *199*(1), 331–406. https://doi.org/10.1007/s11214-016-0245-4

Raptis, S., Lalti, A., Lindberg, M., Turner, D. L., Caprioli, D., & Burch, J. L. (2025a). Revealing an unexpectedly low electron injection threshold via reinforced shock acceleration. *Nature Communications*, *16*(1), 488. https://doi.org/10.1038/s41467-024-55641-9

Raptis, S., Lindberg, M., Liu, T. Z., Turner, D. L., Lalti, A., Zhou, Y., et al. (2025b). Multimission observations of relativistic electrons and high-speed jets linked to shock-generated transients. *The Astrophysical Journal Letters*, *981*(1), L10. https://doi.org/10.3847/2041-8213/adb154

Russell, C. T., Anderson, B. J., Baumjohann, W., Bromund, K. R., Dearborn, D., Fischer, D., et al. (2016). The magnetospheric multiscale magnetometers. *Space Science Reviews*, *199*(1), 189–256. https://doi.org/10.1007/s11214-014-0057-3

Santolík, O., Parrot, M., & Lefeuvre, F. (2003). Singular value decomposition methods for wave propagation analysis. *Radio Science*, *38*(1), 10-1–10-13. https://doi.org/10.1029/2000RS002523

Shi, X. (2024). Diffusion coefficient. *Zenodo*. https://doi.org/10.5281/zenodo.13910524

Shi, X., Artemyev, A., Angelopoulos, V., Liu, T., & Wilson, L. B. III. (2025). Compound electron acceleration at planetary foreshocks. *Nature Communications*, *16*(1), 77. https://doi.org/10.1038/s41467-024-55464-8

Shue, J.-H., Song, P., Russell, C., Steinberg, J., Chao, J., Zastenker, G., et al. (1998). Magnetopause location under extreme solar wind conditions. *Journal of Geophysical Research*, *103*(A8), 17691–17700. https://doi.org/10.1029/98ja01103

Sperveslage, K., Neubauer, F., Baumgärtel, K., & Ness, N. (2000). Magnetic holes in the solar wind between 0.3 au and 17 au. *Nonlinear Processes in Geophysics*, *7*(3/4), 191–200. https://doi.org/10.5194/npg-7-191-2000

Stone, E. C., Frandsen, A. M., Mewaldt, R. A., Christian, E. R., Margolies, D., Ormes, J. F., & Snow, F. (1998). The advanced composition explorer. *Space Science Reviews*, *86*(1–4), 1–22. https://doi.org/10.1023/A:1005082526237

Sulaiman, A. H., Gurnett, D. A., Halekas, J. S., Yates, J. N., Kurth, W. S., & Dougherty, M. K. (2017). Whistler mode waves upstream of Saturn. *Journal of Geophysical Research: Space Physics*, *122*(1), 227–234. https://doi.org/10.1002/2016JA023501

Swanson, D. G. (2020). *Plasma waves* (2nd ed.). CRC Press. https://doi.org/10.1201/9780367802721

Turner, D., Wilson III, L., Liu, T., Cohen, I., Schwartz, S., Osmane, A., et al. (2018). Autogenous and efficient acceleration of energetic ions upstream of earth's bow shock. *Nature*, *561*(7722), 206–210. https://doi.org/10.1038/s41586-018-0472-9

Turner, J., Burlaga, L., Ness, N., & Lemaire, J. (1977). Magnetic holes in the solar wind. *Journal of Geophysical Research*, *82*(13), 1921–1924. https://doi.org/10.1029/ja082i013p01921

Vandas, M. (2001). Shock drift acceleration of electrons: A parametric study. *Journal of Geophysical Research*, *106*(A2), 1859–1871. https://doi.org/10.1029/2000JA900128

Vasko, I. Y., Mozer, F. S., Krasnoselskikh, V. V., Artemyev, A. V., Agapitov, O. V., Bale, S. D., et al. (2018). Solitary waves across supercritical quasi-perpendicular shocks. *Geophysical Research Letters*, *45*(12), 5809–5817. https://doi.org/10.1029/2018GL077835

Webb, G., Axford, W., & Terasawa, T. (1983). On the drift mechanism for energetic charged particles at shocks. *Astrophysical Journal Part 1*, *270*, 537–553. https://doi.org/10.1086/161146

Wilson, L. B., Sibeck, D. G., Turner, D. L., Osmane, A., Caprioli, D., & Angelopoulos, V. (2016). Relativistic electrons produced by foreshock disturbances observed upstream of earth's bow shock. *Physical Review Letters*, *117*(21), 215101. https://doi.org/10.1103/PhysRevLett.117.215101

Wu, C. S. (1984). A fast fermi process: Energetic electrons accelerated by a nearly perpendicular bow shock. *Journal of Geophysical Research*, *89*(A10), 8857–8862. https://doi.org/10.1029/JA089iA10p08857

Yu, L., Huang, S., Yuan, Z., Jiang, K., Xiong, Q., Xu, S., et al. (2021). Characteristics of magnetic holes in the solar wind revealed by parker solar probe. *The Astrophysical Journal*, *908*(1), 56. https://doi.org/10.3847/1538-4357/abb9a8